Journal of Marine Science and Technology (2018) 23:866–876
https://doi.org/10.1007/s00773-017-0516-0

ORIGINAL ARTICLE

Investigation of linear wave action around a truncated cylinder with non-circular cross section

Jiabin Liu[1,2] · Anxin Guo[1,2] · Qinghe Fang[1,2] · Hui Li[1,2] · Hui Hu[3] · Pengfei Liu[4]

Received: 10 June 2017 / Accepted: 10 December 2017 / Published online: 19 December 2017

Abstract
This paper presents an analytical model to solve the linear wave diffraction problem using a truncated cylinder with an arbitrary smooth cross section. Using the method of separation of variables, the boundary condition equations for the surface of a truncated cylinder are derived. Based on the condition that the radius function of a cylinder surface can be expanded into a Fourier series, the unknown coefficients of the diffraction potential can be obtained from a linear system equation. The surface elevation and wave force are calculated and analyzed in terms of the total velocity potential for different cases. The truncated error introduced in the solving process is discussed. Then, the accuracy of this method is verified by comparison with the results of the boundary element method. Finally, this method is further extended to a practical engineering application with a quasi-ellipse caisson for different drafts and exposures.

Keywords Wave diffraction · Truncated cylinder · Non-circular cross section · Analytical solution · Quasi-ellipse cross section

1 Introduction

Wave action on a floating cylinder is of considerable interest to design engineers and scientists. To estimate the hydrodynamic coefficients thereof, numerous analytical solutions and simulations of diffraction and radiation problems have been researched for decades. Garrett [1] studied the scattering problem of linear waves around a circular dock in finite-depth water using analytical and numerical methods. The analytical method was extended by Yeung [2] to solve the radiation problem for a single truncated cylinder oscillating in finite-depth water and deep water. Bhatta and Rahman [3] used the separation of variables technique to analyze the diffraction and radiation problem for a floating vertical cylinder in finite-depth water and presented the analytical solutions for the surge, heave, and pitch motion cases. Later, the effect of depth-to-radius and draft-to-radius ratios on the hydrodynamic coefficients of the heave motion of a vertical cylinder was studied by Bhatta [4]. Based on previous studies, Finnegan et al. [5] presented an approximation analytical expression for a floating vertical cylinder in water of infinite depth. His results were verified by comparison with the experimental results obtained by Fonseca et al. [6]. For the case of extremely shallow water, Drobyshevski [7] derived a closed asymptotic formula to study the hydrodynamic coefficients of a floating cylinder. A set of theoretical added mass, damping coefficient, and exciting force expressions is given for the heave, surge, and pitch motions. Jiang et al. [8, 9] gave the analytical solution to a wave diffraction problem and radiation problem on a submerged vertical cylinder at a finite water depth.

For the diffraction problem of multi-body interaction, a general interaction theory was derived by Kagemoto and Yue [10], which obtains the total potential from the diffraction solutions of individual members. This method was extended by Siddorn and Taylor [11] to investigate the wave

✉ Anxin Guo
guoanxin@hit.edu.cn

1 Key Lab of Structures Dynamic Behavior and Control of the Ministry of Education, Harbin Institute of Technology, Harbin 150090, China

2 Key Lab of Smart Prevention and Mitigation of Civil Engineering Disasters of the Ministry of Industry and Information Technology, Harbin Institute of Technology, Harbin 150090, China

3 Department of Aerospace Engineering, Iowa State University, Ames, IA 50011, USA

4 China Railway Bridge Science Research Institute, Ltd, Wuhan 430034, China

excitation and response of truncated cylinders that are free to oscillate independently, as well as the associated free surface behavior. A complete analysis within a unified framework is provided and discussed in this study.

Regarding the problem of diffraction and radiation around a cylinder over a caisson fixed at the bottom in finite-depth water, Wu et al. [12, 13] presented an analytical approach and studied the added masses, damping coefficients, and exciting forces according to the size of the caisson. Similar problems were analyzed by Hassan and Bora [14], who consider a system consisting of a buoy floating vertically on the free surface above a bottom-mounted caisson. Further work was conducted with two coaxial vertical cylinders, where one is a riding hollow cylinder and the other a solid cylinder of greater radius, at some distance above an impermeable horizontal bottom [15].

An analytical model using an imaging method [16] for the three-dimensional wave diffraction and radiation problem of a floating cylinder located in front of a vertical wall at a finite water depth was formulated [17, 18]. The influence of the distance between the cylinder and vertical wall, draft of the cylinder, and water depth on the hydrodynamic coefficients is discussed.

However, to the best of the authors' knowledge, analytical studies of the diffraction problem around a truncated cylinder with an arbitrary section have seldom been attempted. With the demands of offshore engineering, such a study is required. For instance, during the construction period of the new Tacoma Narrows Bridge [19], the caisson was floated in the river using buoyancy and moored in place to resist wave and current action. The security of the floating caisson in the construction period is significantly affected by its hydrostatic and hydrodynamic properties. Although the boundary element method can solve these problems accurately and effectively, an analytical solution is still necessary to provide a reference in terms of numerical results.

The method presented in this paper allows the solution for the linear diffraction problem of a truncated cylinder with arbitrary cross section. The present study follows from the authors' previous work [20]. The solving process is the same as that used by Bhatta and Rahman [3], where the unknown coefficient can be determined from the boundary conditions by expanding the radius function of a truncated cylinder into a Fourier series. The analytical solution for diffracted potentials is obtained, and the wave elevation and wave excitation forces for different cases are then calculated using the present analytical model. The accuracy of the method presented in this paper is verified by comparing with the results of the numerical method. A practical example was demonstrated with a quasi-ellipse caisson, which is frequently used as the foundation of cross-strait bridges.

2 Formulation of the hydrodynamic problem

Figure 1 shows a schematic of the wave diffraction around a truncated cylinder with an arbitrary smooth section. In the following analysis, the origin of the global coordinate system is fixed on the still water lever with the z-axis pointing vertically upward. The polar coordinate (r, θ, z) of the truncated cylinder is set inside the cross section. The cylinder is exposed to a plane wave with a frequency σ and linear amplitude A, propagating in the positive direction of the x-axis. In this study, it was assumed that the radius function for the cross section could be expanded into a Fourier series based on the assumption of a smooth cylinder surface. The water depth is h and the draft of the truncated cylinder is b. The radius function $r(\theta)$ for the cross section of the cylinder in the local polar coordinate can be written as:

$$r(\theta) = \sum_{n_r=-\infty}^{\infty} b_{n_r} \mathrm{e}^{in_r\theta}, \tag{1}$$

where $n_r \in Z$.

The surface function, S, for the truncated cylinder can be given by:

$$S(r, \theta) = r - \sum_{n_r=-\infty}^{\infty} b_{n_r} \mathrm{e}^{in_r\theta}. \tag{2}$$

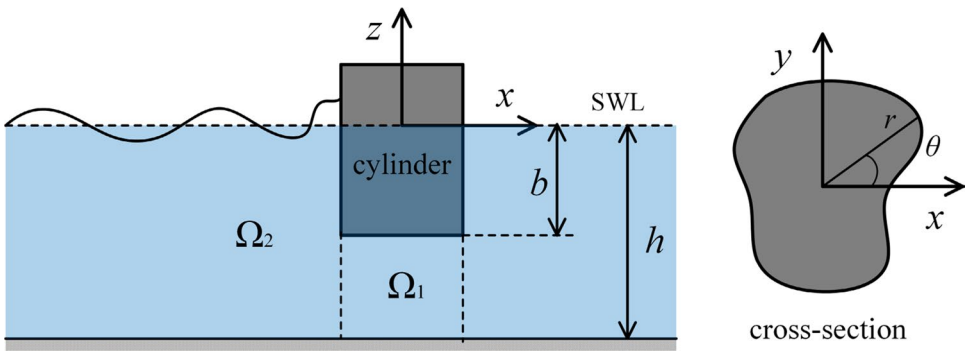

Fig. 1 Definition sketch for the diffraction problem of a truncated vertical cylinder

As in the studies by Yeung [2] and Bhatta and Rahman [3], the fluid domain is divided into an interior region $\Omega_1(S \leqslant 0, \ -h \leqslant z \leqslant -b)$ and an exterior region $\Omega_2(S \geqslant 0, \ -h \leqslant z \leqslant 0)$.

The velocity potential of the fluid with a linear assumption should satisfy Laplace's equation and the corresponding boundary conditions. Herein, the governing equation and boundary conditions for the wave potential are summarized as follows:

Laplace's equation:

$$\nabla^2\Phi=0. \tag{3}$$

Free surface condition ($z = 0$):

$$\frac{\partial\Phi}{\partial z} - \frac{\sigma^2}{g}\Phi = 0, \tag{4}$$

where g is the gravitational acceleration.

Seabed condition ($z = -h$):

$$\frac{\partial\Phi}{\partial z} = 0. \tag{5}$$

Cylinder surface condition:

$$\nabla\Phi \cdot \vec{\mathbf{n}}_{\mathbf{s}} = 0, \tag{6}$$

where $\vec{\mathbf{n}}_{\mathrm{s}}$ is the normal vector on the surface of the cylinder.

The total velocity potential can be written in the following form:

$$\Phi(r, y, \theta, t) = \phi(r, \theta, z)\mathrm{e}^{-i\sigma t}, \tag{7}$$

where

$$\phi = \phi_S^{\mathrm{i}} \ (\Omega_1); \ \ \phi = \phi_{\mathrm{I}} + \phi_S^{\mathrm{e}} \ (\Omega_2), \tag{8}$$

in which ϕ_{I} represents the velocity potential of the incident wave in the exterior region; ϕ_S^{e} and ϕ_S^{i} represent the velocity potential of the diffraction wave in the exterior and interior regions, respectively.

The incident wave potential in the polar coordination system is:

$$\phi_{\mathrm{I}}^{\mathrm{e}} = -i\frac{gA}{\sigma}\frac{\cosh\lambda_0(z+h)}{\cosh\lambda_0 h}\sum_{m=-\infty}^{\infty} J_m(\lambda_0 r)\cdot \mathrm{e}^{im\frac{\pi}{2}}\mathrm{e}^{im\theta}, \tag{9}$$

in which $J_m(\cdot)$ is a first-kind Bessel function with order m. λ_0 satisfies the relation $\sigma^2 = \lambda_0 g\tanh(\lambda_0 h)$.

The diffraction wave potentials ϕ_S^{e} and ϕ_S^{i} have different forms in the exterior and interior regions. Furthermore, the diffraction wave ϕ_S^{e} in the exterior region should also satisfy the Sommerfeld radiation condition at the far field:

$$\lim_{r\to\infty}\sqrt{r}\left(\frac{\partial\phi_S^{\mathrm{e}}}{\partial r} - ik\phi_S^{\mathrm{e}}\right) = 0. \tag{10}$$

The diffraction wave ϕ_S^{e} in the exterior region can be constructed as follows:

$$\phi_S^{\mathrm{e}} = -i\frac{gA}{\sigma}\sum_{m=-\infty}^{\infty}\left[\frac{\cosh\lambda_0(z+h)}{\cosh\lambda_0 h}q_{m0}H_m(\lambda_0 r) + \sum_{n=1}^{\infty}\frac{\cos\lambda_j(z+h)}{\cos\lambda_j h}q_{mj}K_m(\lambda_j r)\right]\cdot \mathrm{e}^{im\theta}, \tag{11}$$

where q_{mn} ($n = 0, 1, 2, \ldots$) represents unknown constants; $H_m(\cdot)$ is the Hankel function of the first kind and $K_m(\cdot)$ is the modified Bessel function of the second kind with order m; λ_j satisfies the relation $\sigma^2=\lambda_0 g\tanh(\lambda_0 h) = -\lambda_j g\tan(\lambda_j h)$ $(j = 1, 2, \ldots)$ Hence, the set of functions $\{\cosh\lambda_0(z+h), \ \cos\lambda_j(z+h)\}$, $j = 1, 2, \ldots$ could form an orthogonal set defined in the interval $-h \leqslant z \leqslant 0$, and the orthonormal set can be constructed provided:

$$Z_{\lambda_0}(z) = N_{\lambda_0}^{-1/2}\cosh\lambda_0(z+h), \tag{12}$$

$$Z_{\lambda_j}(z) = N_{\lambda_j}^{-1/2}\cos\lambda_j(z+h), \tag{13}$$

where

$$N_{\lambda_0} = \frac{1}{2}\left[1 + \frac{\sinh 2\lambda_0 h}{2\lambda_0 h}\right], \tag{14}$$

$$N_{\lambda_j} = \frac{1}{2}\left[1 + \frac{\sin 2\lambda_j h}{2\lambda_j h}\right]. \tag{15}$$

The diffraction wave velocity potential in the interior region can be constructed as follows [11]:

$$\phi_S^{\mathrm{i}} = -i\frac{gA}{\sigma}\sum_{m=-\infty}^{\infty}\left[p_{m0}r^{|m|} + \sum_{n=1}^{\infty}p_{mn}I_m(k_n r)\cos k_n(z+h)\right]\cdot \mathrm{e}^{im\theta}, \tag{16}$$

where p_{mn} ($n = 0, 1, 2, \ldots$) represents unknown constants, $k_n = n\pi/(h-b)$ represents the eigenvalues, and $I_m(\cdot)$is the modified Bessel function of the first kind with order m.

In polar coordinates, the normal vector, $\vec{\mathbf{n}}_{\mathrm{s}}$, on the side surface of the cylinder is given by:

$$\vec{\mathbf{n}}_{\mathrm{s}} = \frac{1}{\sqrt{1+\left(\frac{1}{r}\frac{\partial S}{\partial\theta}\right)^2}}\begin{pmatrix} 1 & \frac{1}{r}\frac{\partial S}{\partial\theta} & 0\end{pmatrix}, \tag{17}$$

where $\frac{\partial S}{\partial\theta} = -\sum_{n_r=-\infty}^{\infty} in_r b_{n_r}\mathrm{e}^{in_r\theta}$.

The boundary conditions are:

$$\left(r^2\frac{\partial\phi_S^{\mathrm{e}}}{\partial r}+\frac{\partial S}{\partial\theta}\frac{\partial\phi_S^{\mathrm{e}}}{\partial\theta}\right)\Big|_{S=0}+\left(r^2\frac{\partial\phi_{\mathrm{I}}^{\mathrm{e}}}{\partial r}+\frac{\partial S}{\partial\theta}\frac{\partial\phi_{\mathrm{I}}^{\mathrm{e}}}{\partial\theta}\right)\Big|_{S=0}=0, \tag{18}$$

with $-b\leqslant z\leqslant 0$, and

$$\phi_S^{\mathrm{e}}+\phi_{\mathrm{I}}^{\mathrm{e}}=\phi_S^{\mathrm{i}}, \tag{19}$$

$$\left(r^2\frac{\partial\phi_S^{\mathrm{e}}}{\partial r}+\frac{\partial S}{\partial\theta}\frac{\partial\phi_S^{\mathrm{e}}}{\partial\theta}\right)\Big|_{S=0}+\left(r^2\frac{\partial\phi_{\mathrm{I}}^{\mathrm{e}}}{\partial r}+\frac{\partial S}{\partial\theta}\frac{\partial\phi_{\mathrm{I}}^{\mathrm{e}}}{\partial\theta}\right)\Big|_{S=0}=\left(r^2\frac{\partial\phi_S^{\mathrm{i}}}{\partial r}+\frac{\partial S}{\partial\theta}\frac{\partial\phi_S^{\mathrm{i}}}{\partial\theta}\right)\Big|_{S=0}, \tag{20}$$

with $-h\leqslant z\leqslant -b$.

To determine the coefficients p_{mn} and q_{mn} in the above equation, the Hankel function, Bessel function, modified Bessel functions and their derivatives are expanded into a Fourier series with $S=0$ as follows:

$$H_m(\lambda_0 r)\big|_{S=0}=\sum_{q_r=-\infty}^{\infty}d_{mq_r}\mathrm{e}^{iq_r\theta},\qquad H'_m(\lambda_0 r)\big|_{S=0}=\sum_{q_r=-\infty}^{\infty}\tilde{d}_{mq_r}\mathrm{e}^{iq_r\theta}, \tag{21}$$

$$J_m(\lambda_0 r)\big|_{S=0}=\sum_{q_r=-\infty}^{\infty}f_{mq_r}\mathrm{e}^{iq_r\theta},\qquad J'_m(\lambda_0 r)\big|_{S=0}=\sum_{q_r=-\infty}^{\infty}\tilde{f}_{mq_r}\mathrm{e}^{iq_r\theta}, \tag{22}$$

$$K_m(\lambda_j r)\big|_{S=0}=\sum_{q_r=-\infty}^{\infty}g_{mq_rj}\mathrm{e}^{iq_r\theta},\quad K'_m(\lambda_j r)\big|_{S=0}=\sum_{q_r=-\infty}^{\infty}\tilde{g}_{mq_rj}\mathrm{e}^{iq_r\theta}, \tag{23}$$

$$I_m(\lambda_j r)\big|_{S=0}=\sum_{q_r=-\infty}^{\infty}l_{mq_rj}\mathrm{e}^{iq_r\theta},\quad I'_m(\lambda_j r)\big|_{S=0}=\sum_{q_r=-\infty}^{\infty}\tilde{l}_{mq_rj}\mathrm{e}^{iq_r\theta}. \tag{24}$$

To simplify the derivation process, the function of the radius with $S=0$ can be written as:

$$r^2(\theta)\big|_{S=0}=\sum_{n_r=-\infty}^{\infty}\tilde{b}_{n_r}\mathrm{e}^{in_r\theta},\qquad r^m(\theta)|_{S=0}=\sum_{q_r=-\infty}^{\infty}h_{mq_r}\mathrm{e}^{iq_r\theta}, \tag{25}$$

where $q_r\in Z$.

The Fourier coefficients, d_{mq_r}, $\tilde{d}_{mq_r}$, f_{mq_r}, $\tilde{f}_{mq_r}$, g_{mq_rj}, $\tilde{g}_{mq_rj}$, l_{mq_rj}, $\tilde{l}_{mq_rj}$, $\tilde{b}_{n_r}$ and h_{mq_r}, can be obtained from:

$$\mathfrak{R}_n=\frac{1}{2\pi}\int_{-\pi}^{\pi}\Psi(\theta)\mathrm{e}^{-in\theta}\mathrm{d}\theta, \tag{26}$$

where $\mathfrak{R}_n$ represents the Fourier coefficients and $\Psi(\theta)$ represents the functions to be expanded, which are defined in Eqs. 21–25.

On multiplying Eq. 19 by $2\cos k_{\tilde{n}}(z+h)\big/(h-b)$ on both sides and integrating with respect to z over the region of $-h\leqslant z\leqslant -b$, the boundary condition of Eq. 19 becomes

$$\begin{aligned}&\sum_{m=-\infty}^{\infty}\sum_{q_r=-\infty}^{\infty}\left[\xi_{\lambda_0\tilde{n}}q_{m0}d_{mq_r}+\sum_{j=1}^{\infty}\xi_{\lambda_j\tilde{n}}q_{mj}g_{mq_rj}\right]\cdot\mathrm{e}^{i(m+q_r)\theta}\\&+\sum_{m=-\infty}^{\infty}\sum_{q_r=-\infty}^{\infty}\xi_{\lambda_0\tilde{n}}f_{mq_r}\cdot\mathrm{e}^{im\frac{\pi}{2}}\mathrm{e}^{i(m+q_r)\theta}\\&=\sum_{m=-\infty}^{\infty}\sum_{q_r=-\infty}^{\infty}\left[2p_{m0}h_{mq_r}\delta_{0\tilde{n}}+(1-\delta_{0\tilde{n}})p_{m\tilde{n}}l_{mq_r\tilde{n}}\right]\cdot\mathrm{e}^{i(m+q_r)\theta},\end{aligned} \tag{27}$$

where

$$\xi_{\lambda\tilde{n}}=\frac{2}{h-b}\int_{-h}^{-b}\frac{Z_\lambda(z)}{Z_\lambda(0)}\int_{-h}^{-b}\cos k_{\tilde{n}}(z+h)\mathrm{d}z. \tag{28}$$

As a simplification, the substitution of Eqs. 12, 13 into Eq. 28 yields:

$$\xi_{\lambda_0\tilde{n}}=\frac{2\cdot(-1)^n(h-b)\lambda_0\sinh\lambda_0(h-b)}{\{(h-b)^2\lambda_0^2+\tilde{n}^2\pi^2\}\cosh\lambda_0 h}, \tag{29}$$

$$\xi_{\lambda_j\tilde{n}}=\frac{2\cdot(-1)^n(h-b)\lambda_j\sin\lambda_j(h-b)}{\{(h-b)^2\lambda_j^2-\tilde{n}^2\pi^2\}\cos\lambda_j h}. \tag{30}$$

Equation 27 can be rewritten as a linear system of equations according to the functions of $\mathrm{e}^{i\tilde{m}\theta}$ as follows:

$$L_{\tilde{m}}(q_{mn},p_{mn})\mathrm{e}^{i\tilde{m}\theta}=R_{\tilde{m}}\mathrm{e}^{i\tilde{m}\theta},\quad(\tilde{m}=-\infty,\ldots,+\infty), \tag{31}$$

where $L_{\tilde{m}}(q_{mn},p_{mn})$ represents linear functions composed of unknown constants q_{mn} and p_{mn}; $R_{\tilde{m}}$ represents the coefficients of $\mathrm{e}^{i\tilde{m}\theta}$. To solve the linear system, the order of m, n, and $\tilde{m}$ are truncated at a specific order to balance the accuracy and computational efficiency. Therefore, their ranges in the following calculation are:

$$m=-M,\ \ldots,M;\quad \tilde{m}=-M,\ \ldots,M;\quad \tilde{n}=0,1,\ldots,N_j. \tag{32}$$

Then, Eq. 31 can be organized into the following matrix form:

$$\mathbf{A}_{\tilde{n}}\mathbf{q}+\mathbf{B}_{\tilde{n}}=\mathbf{C}_{\tilde{n}}\mathbf{p}_{\tilde{n}},\quad(\tilde{n}=0,1,\ldots,N_j). \tag{33}$$

The sizes of each matrix are:

$$\begin{array}{ll}\mathbf{A}_{\tilde{n}} & (2M+1)\times((2M+1)\cdot(N_j+1))\\ \mathbf{q} & ((2M+1)\cdot(N_j+1))\times 1\\ \mathbf{B}_{\tilde{n}} & (2M+1)\times 1\\ \mathbf{C}_{\tilde{n}} & (2M+1)\times\ (2M+1)\\ \mathbf{p}_{\tilde{n}} & (2M+1)\times 1\end{array}.$$

Composing the matrices with all values of $\tilde{n}$ yields:

$$\mathbf{Aq} + \mathbf{B} = \mathbf{Cp}, \tag{34}$$

where

$$\mathbf{A} = \begin{bmatrix} \mathbf{A}_0 \\ \mathbf{A}_1 \\ \vdots \\ \mathbf{A}_{N_j} \end{bmatrix}, \quad \mathbf{B} = \begin{bmatrix} \mathbf{B}_0 \\ \mathbf{B}_1 \\ \vdots \\ \mathbf{B}_{N_j} \end{bmatrix}, \quad \mathbf{C} = \begin{bmatrix} \mathbf{C}_0 & & & \\ & \mathbf{C}_1 & & \\ & & \ddots & \\ & & & \mathbf{C}_{N_j} \end{bmatrix}, \tag{35}$$

$$\mathbf{q} = \begin{bmatrix} \mathbf{q}_0 & \mathbf{q}_1 & \cdots & \mathbf{q}_{N_j} \end{bmatrix}^T, \quad \mathbf{q}_j = \begin{bmatrix} q_{(-M)j} & \cdots & q_{Mj} \end{bmatrix}, \tag{36}$$

$$\mathbf{p} = \begin{bmatrix} \mathbf{p}_0 & \mathbf{p}_1 & \cdots & \mathbf{p}_{N_j} \end{bmatrix}^T, \quad \mathbf{p}_j = \begin{bmatrix} p_{(-M)j} & \cdots & p_{Mj} \end{bmatrix}. \tag{37}$$

Then, matrix $\mathbf{p}$ can be represented by $\mathbf{q}$ as follows:

$$\mathbf{p} = \mathbf{C}^{-1}(\mathbf{Aq} + \mathbf{B}). \tag{38}$$

The boundary conditions of Eqs. 18 and 20 are translated by multiplying with Z_τ / h on both sides and integrating with respect to z over the regions $-b \leqslant z \leqslant 0$ and $-h \leqslant z \leqslant -b$, respectively. Next, the addition of the translation results yields:

$$\begin{aligned} &\sum_{n_r=-\infty}^{\infty}\sum_{q_r=-\infty}^{\infty}\sum_{m=-\infty}^{\infty}\left[\begin{aligned}&\frac{\delta_{\lambda_0\tau}}{Z_{\lambda_0}(0)}\left(\tilde{b}_{n_r}\lambda_0\tilde{d}_{q_r} + mn_r b_{n_r} d_{q_r}\right)q_{m0} \\ &+\sum_{j=1}^{\infty}\frac{\delta_{\lambda_j\tau}}{Z_{\lambda_j}(0)}\left(\tilde{b}_{n_r}\lambda_j\tilde{g}_{q_r j} + mn_r b_{n_r} g_{q_r j}\right)q_{mj}\end{aligned}\right]\cdot \mathrm{e}^{i(m+q_r+n_r)\theta} \\ &+\sum_{n_r=-\infty}^{\infty}\sum_{q_r=-\infty}^{\infty}\sum_{m=-\infty}^{\infty}\frac{\delta_{\lambda_0\tau}}{Z_{\lambda_0}(0)}\mathrm{e}^{im\frac{\pi}{2}}\left[\tilde{b}_{n_r}\lambda_0\tilde{f}_{q_r} + mn_r b_{n_r} f_{q_r}\right]\cdot \mathrm{e}^{i(m+q_r+n_r)\theta} \\ &=\sum_{n_r=-\infty}^{\infty}\sum_{q_r=-\infty}^{\infty}\sum_{m=-\infty}^{\infty}\left[\begin{aligned}&\left(\tilde{b}_{n_r}|m|h_{(m-1)q_r} + mn_r b_{n_r} h_{mq_r}\right)\varsigma_{\tau 0}p_{m0} + \\ &\sum_{n=1}^{\infty}\left(\tilde{b}_{n_r}k_n\tilde{l}_{mq_r j} + mn_r b_{n_r} l_{mq_r j}\right)\varsigma_{\tau n}p_{mn}\end{aligned}\right]\cdot \mathrm{e}^{i(m+q_r+n_r)\theta}, \end{aligned} \tag{39}$$

where

$$\varsigma_{\tau n} = \frac{1}{h}\int_{-h}^{-b} Z_\tau(z)\cos k_n(z+h)\mathrm{d}z. \tag{40}$$

Comparison with Eq. 28 gives the following relation:

$$\varsigma_{\tau n} = \frac{Z_\tau(0)(h-b)}{2h}\xi_{\tau n}. \tag{41}$$

Then, Eq. 39 can be organized into the following matrix form:

$$\mathbf{D}_\tau\mathbf{q} + \mathbf{E}_\tau = \mathbf{F}_\tau\mathbf{p}, \quad (\tau = 0, 1, \ldots, N_j). \tag{42}$$

The sizes of each matrix are:

$$\begin{aligned} &\mathbf{D}_\tau \ \ (2M+1)\times((2M+1)\cdot(N_j+1)) \\ &\mathbf{E}_\tau \ \ (2M+1)\times 1 \\ &\mathbf{F}_\tau \ \ (2M+1)\times((2M+1)\cdot(N_j+1)) \end{aligned}.$$

Composing the matrices with all values of τ yields:

$$\mathbf{Dq} + \mathbf{E} = \mathbf{Fp}, \tag{43}$$

where

$$\mathbf{D} = \begin{bmatrix} \mathbf{D}_0 \\ \mathbf{D}_1 \\ \vdots \\ \mathbf{D}_{N_j} \end{bmatrix}, \quad \mathbf{E} = \begin{bmatrix} \mathbf{E}_0 \\ \mathbf{E}_1 \\ \vdots \\ \mathbf{E}_{N_j} \end{bmatrix}, \quad \mathbf{F} = \begin{bmatrix} \mathbf{F}_0 \\ \mathbf{F}_1 \\ \vdots \\ \mathbf{F}_{N_j} \end{bmatrix}. \tag{44}$$

Substituting Eq. 38 into Eq. 43 yields:

$$\mathbf{Dq} + \mathbf{E} = \mathbf{FC}^{-1}(\mathbf{Aq} + \mathbf{B}). \tag{45}$$

Finally, matrix $\mathbf{q}$ can be obtained from the follow equation:

$$\mathbf{q} = (\mathbf{D} - \mathbf{FC}^{-1}\mathbf{A})^{-1}(\mathbf{FC}^{-1}\mathbf{B} - \mathbf{E}). \tag{46}$$

and $\mathbf{p}$ can be obtained from Eq. 38.

Once matrices $\mathbf{p}$ and $\mathbf{q}$ are obtained, the velocity potential of the incident and diffraction waves in the exterior and interior regions can be obtained. With the velocity potential, the free surface elevation can be computed by:

$$\eta(r,\theta,t) = \mathrm{Re}\left\{-\frac{1}{g}\frac{\partial\Phi}{\partial t}\bigg|_{z=0}\right\}. \tag{47}$$

The pressure in the fluid domain is given by:

$$P(r,\theta,z,t) = -\rho g z - \rho\,\mathrm{Re}\left\{\frac{\partial\Phi}{\partial t}\right\}. \tag{48}$$

With the pressure applied on the cylinder, as shown in Fig. 2, the vibration wave forces acting on the cylinder along the x- and y-axes are then computed by:

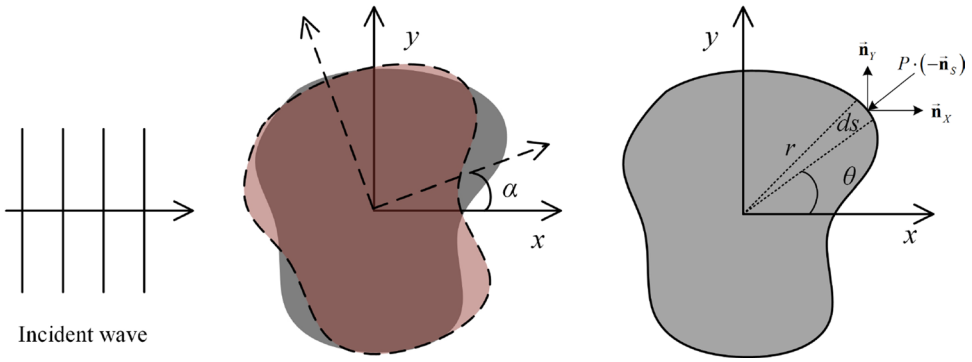

Fig. 2 Definition of the rotation angle and pressure vector on the cylinder surface

$$\bar{F}_X = \int_{-b}^{0} \int_{S=0} P(-\vec{\mathbf{n}}_S) \cdot \vec{\mathbf{n}}_X \mathrm{d}s\mathrm{d}z, \tag{49}$$

$$\bar{F}_Y = \int_{-b}^{0} \int_{S=0} P(-\vec{\mathbf{n}}_S) \cdot \vec{\mathbf{n}}_Y \mathrm{d}s\mathrm{d}z, \tag{50}$$

in which $\vec{\mathbf{n}}_X$ and $\vec{\mathbf{n}}_Y$ are unit vectors along the x- and y-axes, respectively. In the following equation, a dimensionless hydrodynamic force related to the vibration amplitude is adopted in the analysis.

$$F_X = \frac{\bar{F}_{X\text{-am}}}{\rho g A \pi a_0^2}; \quad F_Y = \frac{\bar{F}_{Y\text{-am}}}{\rho g A \pi a_0^2}, \tag{51}$$

in which a_0 is the coefficient of $\mathrm{e}^{in\theta}$ $(n = 0)$ in Eq. 1. The dimensionless bending moment along the x- and y-axis is defined as:

$$M_X = \frac{\bar{M}_X\text{-am}}{\rho g A \pi a_0^2 h}; \quad M_Y = \frac{\bar{M}_Y\text{-am}}{\rho g A \pi a_0^2 h}. \tag{52}$$

In Eq. 51 and 52, $\overline{F}_{X \text{ or } Y\text{-am}}$ and $\overline{M}_{X \text{ or } Y\text{-am}}$ are the vibration amplitude of the wave force and bending moment along the x- or y-axis.

The dimensionless wave run-up can also be defined as:

$$R = \Delta_{\max}/A \tag{53}$$

in which $\Delta_{\max}$ is the wave run-up around the cylinder surface.

3 Validation and case study

3.1 Validation

A vertical truncated cylinder with cosine-type radial perturbations is used to validate the present method. The geometric surface of such a section is expressed by the radius function of the cross section as:

$$r(\theta) = a_0\big(1 + \varepsilon \cos n_r(\theta - \alpha)\big), \tag{54}$$

in which a_0 is the radius of the circular section, ε is the perturbation value of the radius, and α is the rotation angle, as shown in Fig. 2.

In the calculation process, the order, q_r, needs to be truncated to an order N_q. To analyze the effect of the truncation error on q_r, a relative error function is defined as follows:

$$E_\Psi = \frac{\int_{-\pi}^{\pi} \left|\Psi(\theta) - \sum_{n=-N_q}^{N_q} \Re_n e^{in\theta}\right|^2 \mathrm{d}\theta}{\int_{-\pi}^{\pi} |\Psi(\theta)|^2 \mathrm{d}\theta}, \tag{55}$$

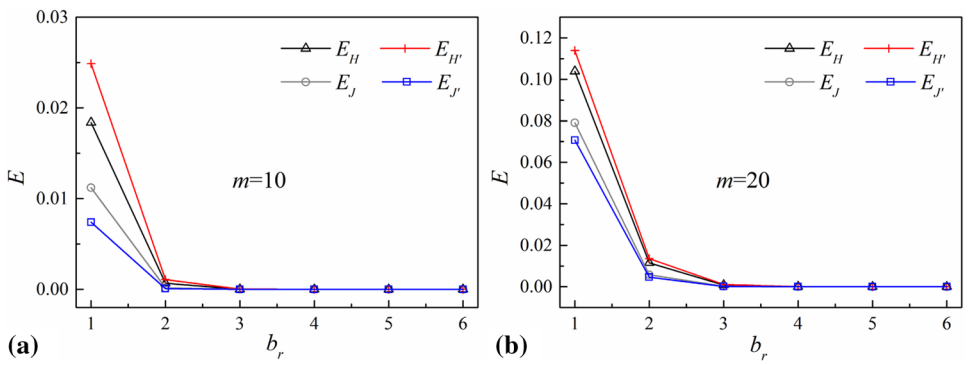

Fig. 3 Convergence of the Fourier series for the first-kind Hankel function, first-kind Bessel function, and their derivation ($n_r = 3$, $\varepsilon = 0.1$, and $\lambda_0 a_0 = 3$). **a** $m = 10$; **b** $m = 20$

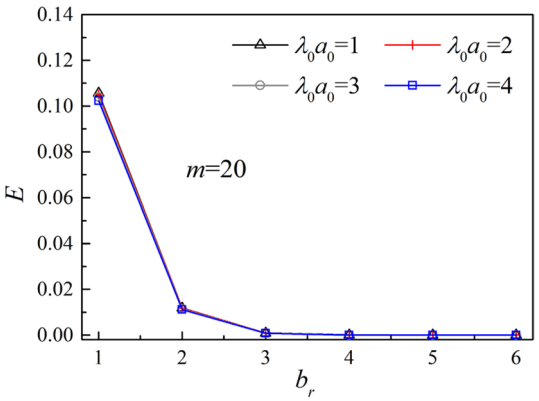

Fig. 4 Convergence of the Fourier series for the first-kind Hankel function, $H_m(\cdot)$ ($n_r = 3$, $\varepsilon = 0.1$, and $m = 20$)

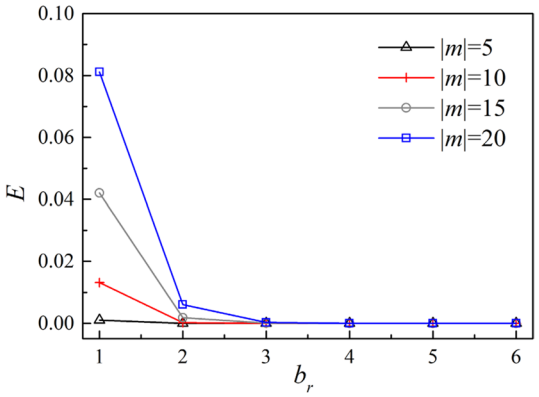

Fig. 5 Convergence of the Fourier series for the radius function, $r^{|m|}$ ($n_r = 3$ and $\varepsilon = 0.1$)

where Ψ and $\mathfrak{R}_n$ are defined in Eq. 26.

To analyze the effect of N_q, an example is given with geometric parameters $n_r = 3$ and $\varepsilon = 0.1$. Figure 3 shows the convergence of the Fourier series for the first-kind Hankel and Bessel functions. The various b_r values shown in this figure are defined by the relation $b_r = N_q/n_r$, and m is the order of the Hankel and Bessel functions. This indicates that the Fourier series can give a good repression of the original function with $b_r = 3$ when $m \leqslant 20$. Figure 4 shows the effect of $\lambda_0 a_0$ on the convergence of the Fourier series for the first-kind Hankel function with $m = 20$, and less effect of it is found in the figure. A similar regulation was found with the modified Bessel function and its derivation, which indicates that the truncated error of the Fourier series can be neglected for $b_r = 3$. The truncated error of the radius function, $r^{|m|}(\theta)$, shown in Eq. 16, is shown in Fig. 5. The truncated error converges faster at lower values of m. However, the Fourier series of the radius function still gives a good representation with $b_r = 3$ when $m \leqslant 20$. For the other

Table 1 Effects of the truncated error of F_X with various N_j

$\lambda_0 a_0$	$N_j = 4$	$N_j = 8$	$N_j = 10$	E_4 (%)	E_8 (%)
0.5	0.7103	0.7128	0.7132	0.41	0.06
1.0	0.8858	0.8880	0.8884	0.29	0.05
2.0	0.5782	0.5789	0.5790	0.14	0.02
3.0	0.3703	0.3705	0.3706	0.08	0.03

$M = 12$, $\varepsilon = 0.1$, and $n_r = 3$. E_i is the error function defined as $|V_i - V_{10}| / V_{10}$, where V_i is the value at $N_j = i$

Table 2 Effects of the truncated error of R with various N_j

$\lambda_0 a_0$	$N_j = 4$	$N_j = 8$	$N_j = 10$	E_4 (%)	E_8 (%)
0.5	1.2746	1.2815	1.2845	0.77	0.23
1.0	1.8087	1.8184	1.8218	0.72	0.19
2.0	2.1436	2.1492	2.1505	0.32	0.06
3.0	2.1622	2.1643	2.1652	0.14	0.04

$M = 12$, $\varepsilon = 0.1$, and $n_r = 3$. E_i is the error function defined as $|V_i - V_{10}| / V_{10}$, where V_i is the value at $N_j = i$

cross section, a convergence analysis is necessary to obtain an accurate value of b_r. The results for this cross section show that $b_r = 3$ is always suitable for the Fourier expansion as the geometry parameters are $n_r \leqslant 4$ and $\varepsilon \leqslant 0.1$.

The truncated error for the orders M and N_j is discussed based on the section used above, which has parameters of $\varepsilon = 0.1$ and $n_r = 3$. The depth-to-radius ratio (h/a_0) is 2, and the draft-to-radius ratio (b/a_0) is 1. The values of F_X and R with various N_j and $\lambda_0 a_0$ are given in Tables 1 and 2, respectively. As shown in these tables, the truncated errors of F_X and R for $N_j = 4$ and $N_j = 8$ are less than 1% compared to the results for $N_j = 10$. This indicates that the analytical results converge in these situations when $N_j \geqslant 4$.

Figure 6 shows the analytical results of F_X and R for different values of M. The order of M has less effect on the wave force, F_X, as shown in Fig. 6a. The analytical results are acceptable, even at $M = 3$. However, the wave run-up is more sensitive than the wave force to the order of M. When $M = 3$, the analytical results have a larger error than the cases when $M = 12$, particularly at higher values of $\lambda_0 a_0$. At orders of M up to 9, the results of R closely approximate the results at $M = 12$, as shown in Fig. 6b.

The numerical simulation results obtained from the open source code NEMOH [21], which is a software code for solving the linear hydrodynamic problem of offshore structures, are presented in Figs. 7 and 8 for comparison with the analytical results. Based on the discussion of the truncated error, the parameters for the calculation are $N_j = 4$, $M = 12$, and $b_r = 3$. For the cross section with $\varepsilon = 0.1$ and $n_r = 2$, the analytical results for the wave force and wave run-up are in good agreement with the experimental results, as shown

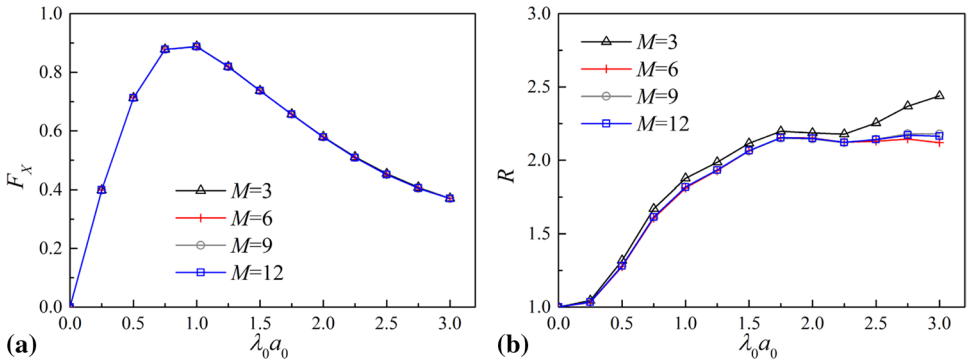

Fig. 6 Effects of the truncated errors for cylinders with various M ($N_j = 8$, $\varepsilon = 0.1$, and $n_r = 3$). **a** Maximum dimensionless wave force in the x-direction and **b** dimensionless wave run-up

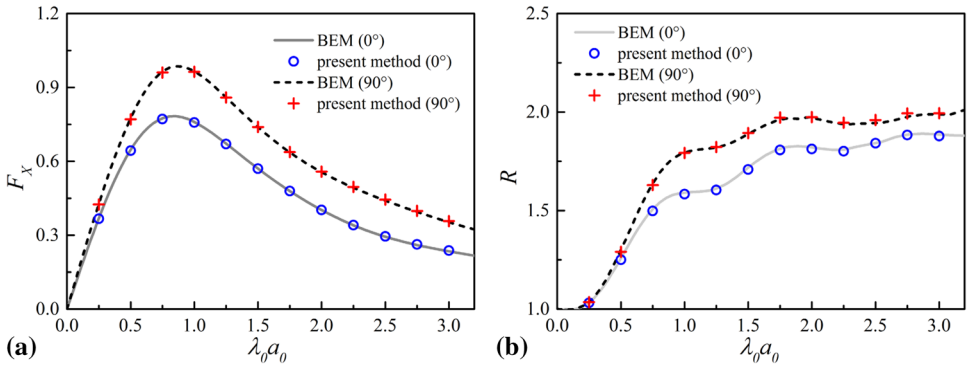

Fig. 7 Comparative results of the cylinder with $\varepsilon = 0.1$ and $n_r = 2$. **a** Maximum dimensionless wave force in the x-direction and **b** maximum dimensionless wave run-up

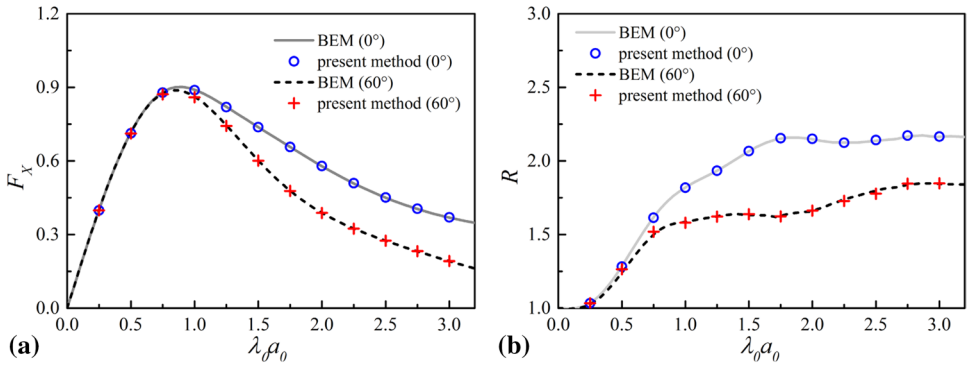

Fig. 8 Comparative results of the cylinder with $\varepsilon = 0.1$ and $n_r = 3$. **a** Maximum dimensionless wave force in the x-direction and **b** maximum dimensionless wave run-up

in Fig. 7a, b. The same conclusion is found in Fig. 8, which concerns the cross section with the parameters $\varepsilon = 0.1$ and $n_r = 3$. The results of the comparisons demonstrate that the present method yields an accurate prediction of wave action on a truncated cylinder.

3.2 Practical example

In the construction process of the caisson foundation for a cross-strait bridge, engineers first construct the caisson in the harbor. Then, the uncompleted caisson is dragged to the construction site by tugboats. It is floated in water using the balance of gravity and buoyancy. With continued construction, the caisson sinks gradually until it reaches the seabed. The period over which the foundation floats on the water represents a dangerous situation that involves wave forces. In this subsection, the wave force and wave run-up of a quasi-ellipse caisson foundation for a cross-strait bridge pylon, which is floating in the ocean, are analyzed using the present method. The schematic of the foundation is shown in Fig. 9. The caisson foundation has an approximately elliptical section with dimensions of 60 × 80 m, combining a central rectangle of 20 × 60 m and two external half circles with a radius of 30 m.

The water depth, h, at the construction site of the bridge is 46.64 m. The extreme sea state with a return period of 25 years is used for the structural design according to meteorological and hydrological data. The wave period, T, and

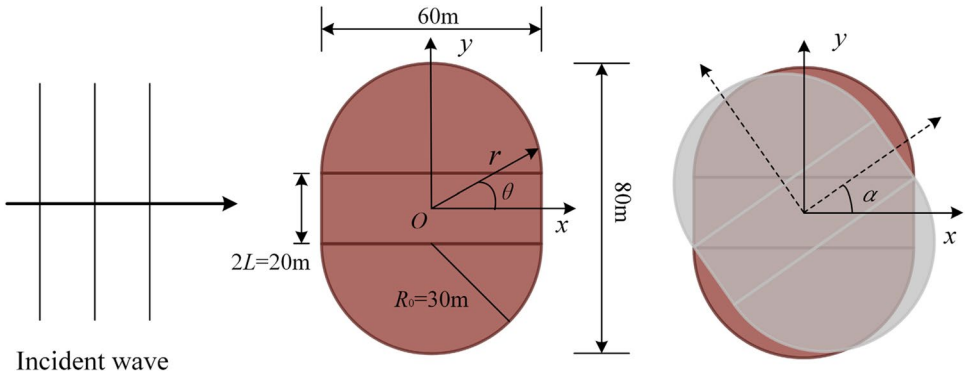

Fig. 9 Schematic of the caisson foundation

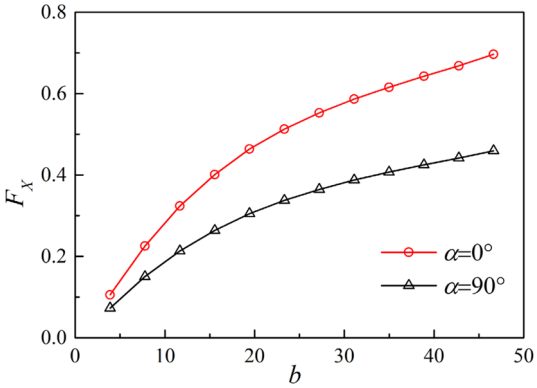

Fig. 10 Dimensionless wave force versus different drafts

the wave height, H, corresponding to the extreme sea state are 8.7 s and 7.1 m, respectively. The wave number for the sea state can be calculated easily as 0.0539 rad/m. To investigate the influence of drafts on the wave action, twelve types of drafts ranging from 11.64 to 46.64 m are evaluated in the following calculation. By a convergence analysis of this case, it showed that the truncated order for n_r can be set as 14 to obtain an accurate representation of original cross section. From the convergence analysis, it is found that the wave force and wave run-up are acceptable with $b_r = 2$, $N_j = 8$ and $M = 34$, respectively. Therefore, those parameters described above are adopted for the following analysis.

The results for the dimensionless wave force with two different rotation angles, $\alpha = 0°$ and 90°, for each draft are shown in Fig. 10. It is clear that the wave force at $\alpha = 0°$ is considerably larger than that at $\alpha = 90°$ as the projected area in the direction of the incident wave is larger at $\alpha = 0°$.

The dimensionless bending moment acting on the structure consists of two parts: wave pressure on the side boundary ($-b \leqslant z \leqslant 0,\ S(r,\theta) = 0$) and bottom boundary ($z = -b,\ r \leqslant r(\theta) = 0$). The tendency of M_Y shown in Fig. 11 is no longer monotonous with the increase in draft. The bending moment first decreases and then increases after the lowest point, which is caused by the difference in phase between the two parts. When the draft value is small, the bending moment is controlled by the second part on the bottom boundary. As the draft increases, the second part decreases gradually, and the first part on the side boundary increases. The dominant parts of the bending moment change with the draft, and the minimum value is close to zero in some situations.

Similar to the wave force in the horizon, the values of the wave run-up around the caisson are larger at $\alpha = 0°$ than at $\alpha = 90°$, as shown in Fig. 12. With increasing draft, the wave run-up for both angles increased consistently. However, the dimensionless results of wave run-up

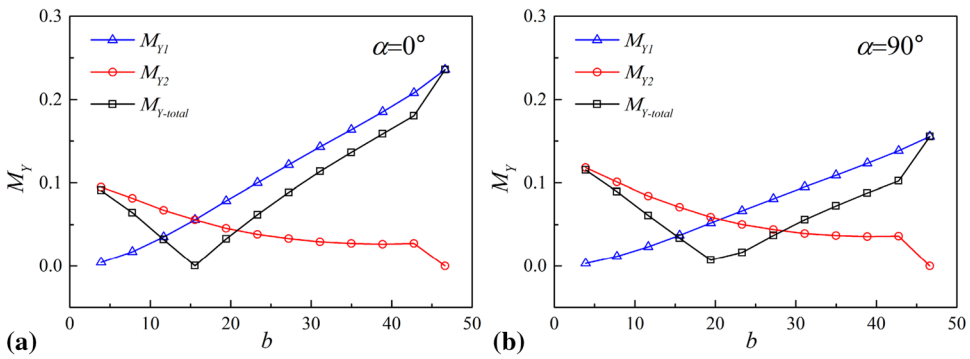

Fig. 11 Dimensionless wave force and wave run-up versus different drafts. **a** Wave force and **b** wave run-up

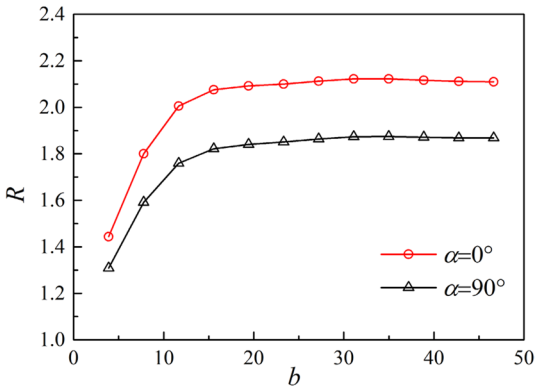

Fig. 12 Dimensionless d wave run-up versus different drafts

increased sharply at the beginning and are less influenced by the draft as $b \geqslant 20$ m.

Figure 13 shows the normalized wave amplitude around the caisson at four different drafts and two angles. As shown, the wave amplitude as a whole for the caisson floating in the water at $b = 11.64$ m is smaller than that of the bottom-mounted cases. The results of the other drafts are similar to the bottom-mounted cases, which means that the effect of the draft is much less when the draft is sufficiently large. Figure 14 shows the 2-D contour plot around the caisson with $\alpha = 0°$ and two different drafts of $b = 11.64$ and 46.64 m, respectively. The major differences between the two drafts occur at the head–body and after-body in the wave direction. A lower wave amplitude is found in these locations for a low value of $b = 11.64$, because incident waves pass under the floating body. A similar conclusion can be drawn from Fig. 15 with $\alpha = 90°$ between the two drafts.

4 Conclusion

An analytical method is presented in this study to investigate the linear wave diffraction around a truncated cylinder with a noncircular cross section. Numerical analysis was carried out to examine the analytical results with different exposures and cross sections. This shows that the present method can successfully predict the wave action on a truncated cylinder with an arbitrary smooth cross

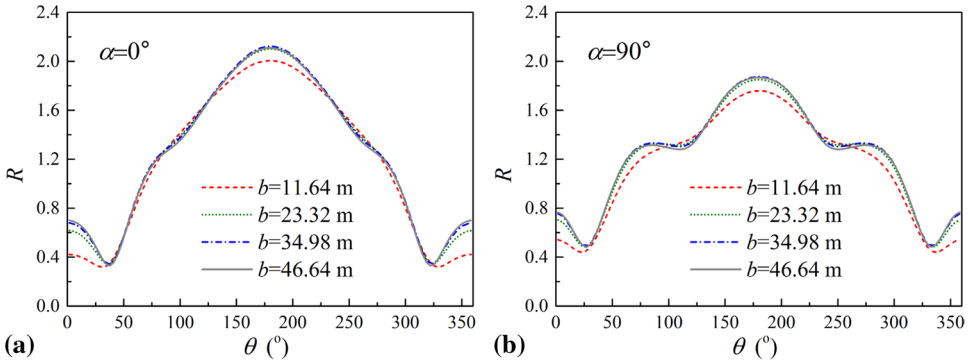

Fig. 13 Dimensionless wave amplitude around the caisson. **a** $\alpha = 0°$ and **b** $\alpha = 90°$

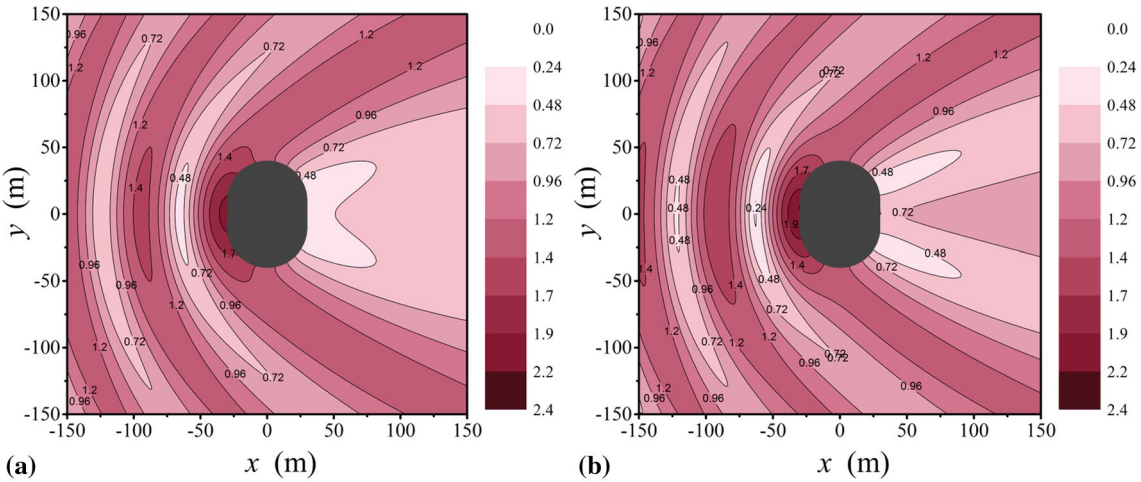

Fig. 14 Contour plot of normalized wave amplitude around caisson. **a** Floating case ($b = 11.64$ m) and **b** bottom-mounted case ($b = 46.64$ m)

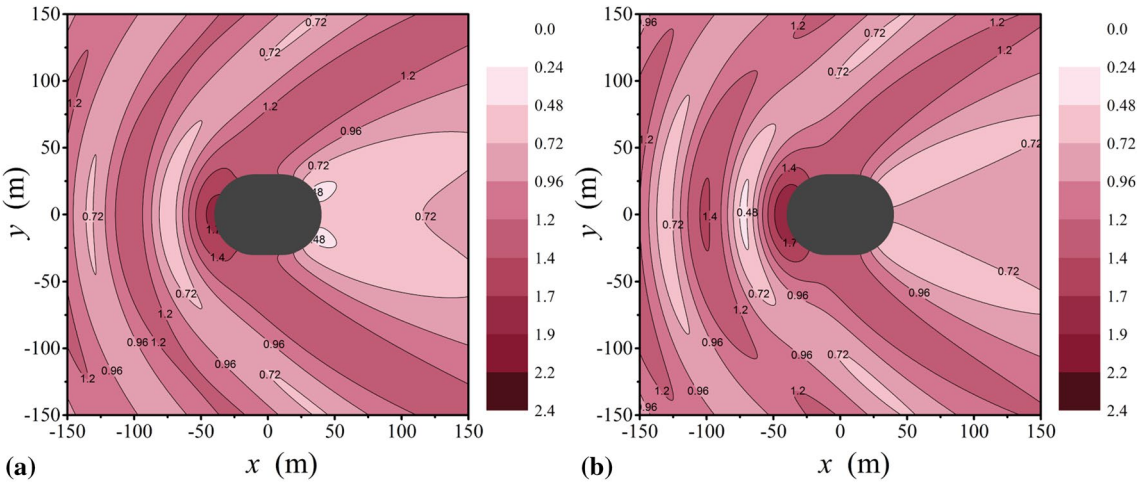

Fig. 15 Contour plot of normalized wave amplitude around caisson. **a** Floating case ($b = 11.64$ m) and **b** bottom-mounted case ($b = 46.64$ m)

section. The wave force and free surface elevation can be obtained easily once the total potential is calculated. To obtain convergence of the final results, the truncated errors were eliminated by increasing the truncated order of the Fourier series. A larger truncated order is required to ensure the accuracy of the final results with increasing wave number. The effect of the draft and rotation angle on the wave force and wave run-up is discussed in terms of a truncated caisson foundation for a bridge pylon. It suggests that the effect of draft on the horizontal wave force would decrease as the increasing of it, and the bending moment can be zero under specific conditions.

Acknowledgements Financial support from the National Natural Science Foundation of China (51725801) is greatly appreciated by the authors.

References

1. Garrett C (1971) Wave forces on a circular dock. J Fluid Mech 46(01):129–139
2. Yeung RW (1981) Added mass and damping of a vertical cylinder in finite-depth waters. Appl Ocean Res 3(3):119–133
3. Bhatta DD, Rahman M (2003) On scattering and radiation problem for a cylinder in water of finite depth. Int J Eng Sci 41(9):931–967
4. Bhatta DD (2007) Computation of added mass and damping coefficients due to a heaving cylinder. J Appl Math Comput 23(1–2):127–140
5. Finnegan W, Meere M, Goggins J (2013) The wave excitation forces on a truncated vertical cylinder in water of infinite depth. J Fluids Struct 40:201–213
6. Fonseca N, Pessoa J, Mavrakos S, Le Boulluec M (2011) Experimental and numerical investigation of the slowly varying wave exciting drift forces on a restrained body in bi-chromatic waves. Ocean Eng 38(17–18):2000–2014
7. Drobyshevski Y (2004) Hydrodynamic coefficients of a floating, truncated vertical cylinder in shallow water. Ocean Eng 31(3–4):269–304
8. Jiang S-C, Gou Y, Teng B, Ning D-Z (2014) Analytical solution of a wave diffraction problem on a submerged cylinder. J Eng Mech 140(1):225–232
9. Jiang SC, Gou Y, Teng B (2014) Water wave radiation problem by a submerged cylinder. J Eng Mech 140(5):06014003
10. Kagemoto H, Yue DK (1986) Interactions among multiple three-dimensional bodies in water waves: an exact algebraic method. J Fluid Mech 166:189–209
11. Siddorn P, Taylor E, R (2008) Diffraction and independent radiation by an array of floating cylinders. Ocean Eng 35(13):1289–1303
12. Wu B-j, Zheng Y-h, You Y-g, Sun X-y, Chen Y (2004) On diffraction and radiation problem for a cylinder over a caisson in water of finite depth. Int J Eng Sci 42(11–12):1193–1213
13. Wu BJ, Zheng YH, You YG, Jie DS, Chen Y (2006) On diffraction and radiation problem for two cylinders in water of finite depth. Ocean Eng 33(5–6):679–704
14. Hassan M, Bora SN (2012) Exciting forces for a pair of coaxial hollow cylinder and bottom-mounted cylinder in water of finite depth. Ocean Eng 50:38–43
15. Hassan M, Bora SN (2013) Exciting forces for a wave energy device consisting of a pair of coaxial cylinders in water of finite depth. J Mar Sci Appl 12(3):315–324
16. Taraldsen G (2005) The complex image method. Wave Motion 43(1):91–97
17. Zheng S, Zhang Y (2015) Wave diffraction from a truncated cylinder in front of a vertical wall. Ocean Eng 104:329–343
18. Zheng S, Zhang Y (2016) Wave radiation from a truncated cylinder in front of a vertical wall. Ocean Eng 111:602–614
19. Chakrabarti SK, Chakrabarti P, Krishna MS (2006) Design, construction, and installation of a floating caisson used as a bridge pier. J Waterw Port Coast Ocean Eng 132(3):143–156
20. Liu J, Guo A, Li H (2016) Analytical solution for the linear wave diffraction by a uniform vertical cylinder with an arbitrary smooth cross-section. Ocean Eng 126:163–175
21. Babarit A, Delhommeau G (2015) Theoretical and numerical aspects of the open source bem solver nemoh, In: 11th wave and tidal energy conference, Nantes European